

PAPER • OPEN ACCESS

## Novel Ni<sub>3</sub>S<sub>4</sub>/NiS/NC composite with multiple heterojunctions synthesized through space-confined effect for high-performance supercapacitors

To cite this article: Wutao Wei *et al* 2023 *Int. J. Extrem. Manuf.* **5** 015504

View the [article online](#) for updates and enhancements.

You may also like

- [Diagnostics of laser-produced Mg plasma through a detailed collisional radiative model with reliable electron impact fine structure excitation cross-sections and self-absorption intensity correction](#)  
S S Baghel, S Gupta, R K Gangwar *et al.*
- [Large-scale synthesis of polyynes with commercial laser marking technology](#)  
Liang Fang, , Yanping Xie *et al.*
- [Interactions between Radio Galaxies and Cluster Shocks. I. Jet Axes Aligned with Shock Normals](#)  
Chris Nolting, T. W. Jones, Brian J. O'Neill *et al.*

# Novel Ni<sub>3</sub>S<sub>4</sub>/NiS/NC composite with multiple heterojunctions synthesized through space-confined effect for high-performance supercapacitors

Wutao Wei<sup>1,2</sup>, Zijie Guo<sup>2</sup>, Jiaqiang Xu<sup>1</sup>, Zhe Fang<sup>2,\*</sup>, JiuJun Zhang<sup>1,\*</sup> , Yu Jia<sup>3</sup> and Liwei Mi<sup>2,\*</sup>

<sup>1</sup> Institute for Sustainable Energy, College of Sciences, Shanghai University, Shanghai 200444, People's Republic of China

<sup>2</sup> Henan Key Laboratory of Functional Salt Materials, Center for Advanced Materials Research, Zhongyuan University of Technology, Zhengzhou 450007, Henan, People's Republic of China

<sup>3</sup> International Laboratory for Quantum Functional Materials of Henan & School of Physics and Engineering, Zhengzhou University, Zhengzhou 450001, Henan, People's Republic of China

E-mail: [zhfang@zut.edu.cn](mailto:zhfang@zut.edu.cn), [jiujun@shaw.ca](mailto:jiujun@shaw.ca) and [mlwzzu@163.com](mailto:mlwzzu@163.com)

Received 9 March 2022, revised 23 March 2022

Accepted for publication 4 December 2022

Published 16 December 2022



CrossMark

## Abstract

The construction of heterojunctions in composite materials to optimize the electronic structures and active sites of energy materials is considered to be the promising strategy for the fabrication of high-performance electrochemical energy devices. In this paper, a one-step, easy processing and cost-effective technique for generating composite materials with heterojunctions was successfully developed. The composite containing Ni<sub>3</sub>S<sub>4</sub>, NiS, and N-doped amorphous carbon (abbreviated as Ni<sub>3</sub>S<sub>4</sub>/NiS/NC) with multiple heterojunction nanosheets are synthesized via the space-confined effect of molten salt interface of recrystallized NaCl. Several lattice matching forms of Ni<sub>3</sub>S<sub>4</sub> with cubic structure and NiS with hexagonal structure are confirmed by the detailed characterization of heterogeneous interfaces. The C-S bonds are the key factor in realizing the chemical coupling between nickel sulfide and NC and constructing the stable heterojunction. Density functional theory calculations further revealed that the electronic interaction on the heterogeneous interface of Ni<sub>3</sub>S<sub>4</sub>/NiS can contribute to high electronic conductivity. The heterogeneous interfaces are identified to be the good electroactive region with excellent electrochemical performance. The synergistic effect of abundant active sites, the enhanced kinetic process and valid interface charge transfer channels of Ni<sub>3</sub>S<sub>4</sub>/NiS/NC multiple heterojunction can guarantee high reversible redox activity and high structural stability, resulting in both high specific capacitance and energy/power densities when it is used as the electrode for supercapacitors. This work offers a new avenue for the rational design of the heterojunction materials with improved electrochemical performance through space-confined effect of NaCl.

\* Authors to whom any correspondence should be addressed.



Original content from this work may be used under the terms of the [Creative Commons Attribution 4.0 licence](https://creativecommons.org/licenses/by/4.0/). Any further distribution of this work must maintain attribution to the author(s) and the title of the work, journal citation and DOI.

Supplementary material for this article is available [online](#)

Keywords: multiple heterojunction, space-confined effect, electronic interaction, supercapacitors

## 1. Introduction

In recent years, the development of new materials for many cutting-edge application areas including electrochemical energy-related devices such as supercapacitors [1, 2], batteries [2, 3], fuel cells [4], water-electrolysis [5–8], and CO<sub>2</sub> electroreduction [5, 6, 8], has become more intensive because of the requirement of clean/sustainable energy storage and conversion. Regarding energy-related materials, optimization of the energy band structure, state density, and electronic structure of the heterojunction interface can endow them with unique functional properties [9, 10]. A heterojunction of material is constructed by the lattice matching of two or more components with different properties through crystal plane coupling. Thus, the heterojunction interface can show the complementary advantages and synergistic effects of different components [11, 12]. For example, heterojunctions between two components can significantly enhance ionic and high electronic conductivity [13–16]. Therefore, heterojunction materials have been recognized as one of the most competitive candidates for applications in energy systems.

Micro- or nano-scale heterojunction materials can be constructed by the corresponding micro/nano fabrication techniques, such as chemical vapor deposition [17–19], ion exchange [13, 20, 21], and hydrothermal and solvothermal methods [22–25]. Currently, most of these synthesis methods involve two or more steps based on gas–solid or liquid-phase reactions [10, 20, 23, 26, 27]. The temperature required for the gas–solid reaction usually reaches the gasification or decomposition temperature of the gas-producing raw material to provide the reaction gas. For example, the temperature needed to produce C<sub>3</sub>N<sub>4</sub> as a promising material for constructing the heterojunction using dicyandiamide and ammonium chloride should reach more than 500 °C [9, 10, 23]. Liquid-phase reactions, such as hydrothermal and solvothermal reactions, usually need to be carried out under high temperature and high pressure in a closed environment [24, 28–30]. Although the commonly reported strategies can construct many unique heterojunction materials with high performance, they still need the assistance of specific equipment, high energy consumption or hazardous operation with high temperature or high pressure, or multi-step complicated operation, which could hinder their practical usage. Therefore, the development of a convenient, cost-efficient, green, and sustainable strategy for the construction of heterojunction materials is required to promote their large-scale application, particularly in electrochemical energy devices such as supercapacitors.

Many studies have been reported in recent years regarding the application of heterojunction materials as electrodes in supercapacitors, including both double-layer supercapacitors and pseudocapacitors [14, 31, 32]. For example, the

synergy of the excellent wettability of N/P co-doped carbon materials in the electrolyte, adequate contact area, and efficient electron transport of one-dimensional (1D) hollow carbon ensures that an N/P co-doped porous carbon/1D hollow tubular carbon heterojunction exhibits a high capacitance of 324 F g<sup>-1</sup> at 1 A g<sup>-1</sup> [33]. Ni<sub>3</sub>S<sub>4</sub> could increase the conductivity of MoS<sub>2</sub> in the Ni<sub>3</sub>S<sub>4</sub>/MoS<sub>2</sub> heterojunction constructed by covering the surface of the Ni<sub>3</sub>S<sub>4</sub> core layer with MoS<sub>2</sub> nanosheets; the impedance of the Ni<sub>3</sub>S<sub>4</sub>/MoS<sub>2</sub> heterojunction was 67% that of pure MoS<sub>2</sub> [34]. A one-body-style photo-supercapacitor based on a Ni(OH)<sub>2</sub>/TiO<sub>2</sub> heterojunction array prepared by the *in-situ* growth of Ni(OH)<sub>2</sub> on TiO<sub>2</sub> nanorods demonstrated that Ni(OH)<sub>2</sub> can store the holes created by TiO<sub>2</sub> under illumination; the release of the holes converts chemical energy into electrical energy during the discharge process, resulting in the direct storage of solar energy [35]. These heterojunction materials strongly promote the development of high-performance or multifunctional supercapacitors by combining materials with different micro/nanostructures and unique photoelectric properties in the form of core–shell or laminated structures. Based on these studies, the electrochemical performance of heterojunction materials can be further improved by constructing multiple heterojunctions within the same nanoscale structural unit.

In this study, a Ni<sub>3</sub>S<sub>4</sub>/NiS/NC (NC: nitrogen-doped amorphous carbon) multiple heterojunction material was synthesized through the space-confined effect of the molten salt interface of recrystallized NaCl. In this strategy, the tight coverage of recrystallized NaCl on the surface of NiCl<sub>2</sub> can be achieved by the coordination of Cl<sup>-</sup> and Ni<sup>2+</sup>. Under the space-confined effect of recrystallized NaCl, the partial exposure of Ni<sup>2+</sup> near the interface of NaCl shows a different reactivity from the complete exposure of Ni<sup>2+</sup>, resulting in contact with different amounts of S<sup>2-</sup> to achieve the one-step controlled construction of the Ni<sub>3</sub>S<sub>4</sub>/NiS heterojunction. Meanwhile, the gas containing carbon and nitrogen in the closed system can be converted into NC under the catalytic action of Ni<sup>2+</sup>, which can further chelate with the Ni<sub>3</sub>S<sub>4</sub>/NiS heterojunction through C–S bonds to form Ni<sub>3</sub>S<sub>4</sub>/NiS/NC multiple heterojunctions. When Ni<sub>3</sub>S<sub>4</sub>/NiS/NC was used as the electrode material for pseudocapacitors, NC first provided direct electron channels and many defects as high-activity reactive sites; it also restricted the structural deformation of nickel sulfide during the reversible pseudocapacitor reaction. In particular, the electron interaction of the Ni<sub>3</sub>S<sub>4</sub>/NiS heterojunction was studied via first-principle calculations based on density functional theory (DFT), and the results revealed increased electronic conductivity at the heterogeneous interface, which can be woven together with NC to form 3D conductive networks within the active materials. Subsequent performance tests on the Ni<sub>3</sub>S<sub>4</sub>/NiS/NC-based

pseudocapacitor demonstrated enhanced electrochemical performance, revealing the advantages of this heterojunction composite material.

## 2. Results and discussion

The detailed regulation strategy is illustrated in figure 1. During the mixing and crushing of  $\text{NiCl}_2 \cdot 6\text{H}_2\text{O}$ ,  $\text{CH}_4\text{N}_2\text{S}$ , and NaCl in an agate mortar, the six crystal  $\text{H}_2\text{O}$  in  $\text{NiCl}_2 \cdot 6\text{H}_2\text{O}$  was removed under the intermolecular forces of NaCl and  $\text{CH}_4\text{N}_2\text{S}$ , resulting in the gradual transformation of a dry green mixture into a wet yellow mixture (figure 1(d)). Up to 35.9 g of NaCl can be dissolved in 100 g of water at room temperature; that is, the mole ratio of NaCl to  $\text{H}_2\text{O}$  in the saturated salt water is 0.11:1. Similarly, according to the mole number of the added material, it was not difficult to obtain a NaCl/ $\text{H}_2\text{O}$  mole ratio of 0.07:1. Thus, the  $\text{H}_2\text{O}$  released by  $\text{NiCl}_2 \cdot 6\text{H}_2\text{O}$  was sufficient to dissolve all NaCl. However,  $\text{NiCl}_2$  and  $\text{CH}_4\text{N}_2\text{S}$  could dissolve only a small fraction. Consequently, the wet yellow mixture contained a core-shell structure of  $\text{NiCl}_2$  and  $\text{CH}_4\text{N}_2\text{S}$  coated with aqueous NaCl (figure 1(a)). The dissolution of NaCl can contribute to the mixed uniformity of the raw materials, and the coordination between  $\text{Cl}^-$  and  $\text{Ni}^{2+}$  induces the preferential adsorption of  $\text{Cl}^-$  on the surface of  $\text{NiCl}_2$ . When the closed system was gradually heated,  $\text{CH}_4\text{N}_2\text{S}$  reacted with  $\text{H}_2\text{O}$  to produce  $\text{CO}_2$ ,  $\text{NH}_3$ , and  $\text{H}_2\text{S}$  (equation (1) in figure 1). The large amount of as-produced gas resulted in the final block material having a porous structure (figures 1(b) and (e)). The molar ratio of  $\text{H}_2\text{O}$  to  $\text{CH}_4\text{N}_2\text{S}$  in the raw material is 2:1, which is the same as the quantitative ratio in equation (1). Therefore, the entire  $\text{CH}_4\text{N}_2\text{S}$  and  $\text{H}_2\text{O}$  in this system were converted to the corresponding gas, which entirely filled the sealed container. However, as shown in equation (1), the molar ratio of NaCl to  $\text{H}_2\text{O}$  gradually increases, resulting in the recrystallization of NaCl on the surface of  $\text{NiCl}_2$  until two solids (NaCl and  $\text{NiCl}_2$ ) and three gases ( $\text{CO}_2$ ,  $\text{NH}_3$  and  $\text{H}_2\text{S}$ ) remain in the system. Based on the eutectic point theory, the microzone of the molten state appears at the interface between NaCl and  $\text{NiCl}_2$ , which is surrounded by  $\text{H}_2\text{S}$  (figure 1(c)). Figures 1(e) and (f) show that three raw materials of  $\text{NiCl}_2 \cdot 6\text{H}_2\text{O}$ ,  $\text{CH}_4\text{N}_2\text{S}$ , and NaCl and two raw materials including  $\text{NiCl}_2 \cdot 6\text{H}_2\text{O}$  and NaCl at 150 °C for 12 h are transformed into hard bulk materials rather than powders, which further proves the formation of a microzone at the interface between NaCl and  $\text{NiCl}_2$ . In the initial stage of the system reaction, the concentration of  $\text{H}_2\text{S}$  is high, resulting in the reaction of  $\text{H}_2\text{S}$  and  $\text{NiCl}_2$  to produce  $\text{Ni}_3\text{S}_4$  (equation (4)), which consumes more  $\text{H}_2\text{S}$  than equation (2). As the reaction of equation (4) proceeds, the concentration of  $\text{H}_2\text{S}$  drops sharply, leading to a decrease in the amount of  $\text{H}_2\text{S}$  around  $\text{NiCl}_2$ . In particular, the space-confined effect of NaCl in the microzone of the molten state can reduce the amount of  $\text{H}_2\text{S}$  contacting  $\text{NiCl}_2$ , resulting in the production of NiS near the interface between NaCl and  $\text{NiCl}_2$  according to equation (2). As the reaction continues, most of the  $\text{NiCl}_2$  is converted into NiS or  $\text{Ni}_3\text{S}_4$ . According to the molar ratio of the raw material, the molar ratio of  $\text{S}^{2-}$  and  $\text{Ni}^{2+}$  in this system

is 3:1. Therefore, there is still abundant  $\text{H}_2\text{S}$  in this closed system, which further triggers equation (3). Then, NiS and  $\text{H}_2\text{S}$  reacts to form  $\text{Ni}_3\text{S}_4$  until the final product of  $\text{Ni}_3\text{S}_4$  with a pure phase is formed. Therefore, a controlled one-step construction of the  $\text{Ni}_3\text{S}_4/\text{NiS}$  heterojunction can be realized by controlling the reaction time under the space-confined effect of recrystallized NaCl. This synthesis strategy can also be extended to the synthesis of other heterojunction materials.

Meanwhile, during the construction of the  $\text{Ni}_3\text{S}_4/\text{NiS}$  heterojunction, a small amount of  $\text{NH}_3$  and  $\text{CO}_2$  in the closed system was converted into NC under the catalytic action of  $\text{Ni}^{2+}$  and this NC could be further chemically coupled with nickel sulfide to form a heterojunction. The combination of  $\text{Ni}_3\text{S}_4/\text{NiS}/\text{NC}$  multiple heterojunctions can introduce many defects, enrich highly active sites, and thus, enhance the kinetic process of the electrochemical reaction [27]. Subsequently, the interface structure of the  $\text{Ni}_3\text{S}_4/\text{NiS}/\text{NC}$  multiple heterojunction was systematically analyzed and characterized. This composite material was successfully used to construct electrodes for supercapacitors that exhibited better electrochemical performance than those fabricated using single-component materials.

X-ray diffraction (XRD) was performed to understand the structural phases of  $\text{Ni}_3\text{S}_4/\text{NiS}/\text{NC}$  formed at different reaction times with the assistance of NaCl, and  $\text{Ni}_3\text{S}_4/\text{NiS}/\text{NC}$ -2,  $\text{Ni}_3\text{S}_4/\text{NiS}/\text{NC}$ -4,  $\text{Ni}_3\text{S}_4/\text{NiS}/\text{NC}$ -8,  $\text{Ni}_3\text{S}_4/\text{NiS}/\text{NC}$ -12,  $\text{Ni}_3\text{S}_4/\text{NiS}/\text{NC}$ -24,  $\text{Ni}_3\text{S}_4/\text{NiS}/\text{NC}$ -36, and  $\text{Ni}_3\text{S}_4/\text{NiS}/\text{NC}$ -48 at the reaction times of 2, 4, 8, 12, 24, 36, and 48 h, respectively. As shown in figure 2(a), the XRD pattern of  $\text{Ni}_3\text{S}_4/\text{NiS}/\text{NC}$ -2 shows distinct diffraction peaks of  $\text{Ni}_3\text{S}_4$  (JCPDS NO. 47-1739) and weak diffraction peaks of NiS (JCPDS NO. 75-0613). Before 12 h, the diffraction peaks of  $\text{Ni}_3\text{S}_4$  and NiS gradually increased as the reaction continued. When the reaction time was more than 12 h, the diffraction peaks of  $\text{Ni}_3\text{S}_4$  were still enhanced, whereas the diffraction peaks of NiS disappeared completely after 36 h. To explore the influence of the space-confined effect of recrystallized NaCl on the composition of the final materials, XRD patterns of the samples synthesized at the reaction times of 6, 8, 12, 24, 36, and 48 h without the assistance of NaCl ( $\text{Ni}_3\text{S}_4/\text{Ni}_3\text{S}_4/\text{NC}$ -6,  $\text{Ni}_3\text{S}_4/\text{NC}$ -8,  $\text{Ni}_3\text{S}_4/\text{NC}$ -12,  $\text{Ni}_3\text{S}_4/\text{NC}$ -24,  $\text{Ni}_3\text{S}_4/\text{NC}$ -36, and  $\text{Ni}_3\text{S}_4/\text{NC}$ -48) are shown in figure S1. The XRD curve of the sample synthesized at 6 h displays very complicated diffraction peaks, which may be related to side reactions in the early stage. For the sample synthesized for 8 h, the complicated diffraction peaks became increasingly weaker, and obvious diffraction peaks of  $\text{Ni}_3\text{S}_4$  appear. When the reaction time reached 12 h, the resulting material was a pure phase of  $\text{Ni}_3\text{S}_4$ . As the reaction continued, only the diffraction peaks of  $\text{Ni}_3\text{S}_4$  were observed in the XRD curves, and the diffraction intensity gradually increased, indicating that the yield of  $\text{Ni}_3\text{S}_4$  gradually improved, and no other hybrid phase could be generated. It is clear that NiS is not formed in the absence of NaCl, further proving that the space-confined effect of NaCl can promote the formation of  $\text{Ni}_3\text{S}_4/\text{NiS}$  heterojunctions. The analysis results of the XRD pattern are consistent with the mechanism of controllable fabrication of the  $\text{Ni}_3\text{S}_4/\text{NiS}$  heterojunction

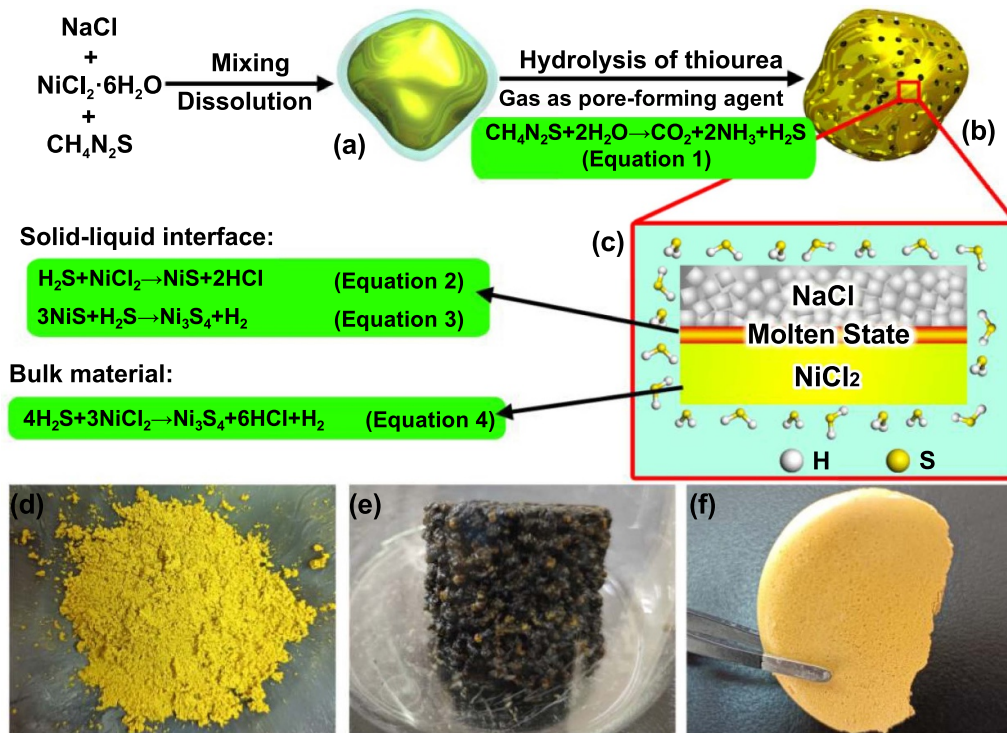


**Figure 1.** Schematic of the controlled synthesis of Ni<sub>3</sub>S<sub>4</sub>/NiS heterojunction by the space-confined effect of molten salt interface of recrystallized NaCl and the photos of the as-obtained materials prepared at different stages. (a) Schematic diagram and (d) photo of material after crushing and mixing. (b) Schematic diagram and (e) photo of the material after the reaction at 150 °C for 12 h. (c) Schematic diagram of the space-confined effect of recrystallized NaCl. (f) Photo of NiCl<sub>2</sub> · 6H<sub>2</sub>O mixed with NaCl and then left at 150 °C for 12 h.

by the space-confined effect of the molten salt interface of recrystallized NaCl, and reveal that Ni<sub>3</sub>S<sub>4</sub>/NiS/NC-12 has the largest recombination ratio of NiS and Ni<sub>3</sub>S<sub>4</sub>.

Figure S2 shows the morphological evolution of Ni<sub>3</sub>S<sub>4</sub>/NiS/NC with the participation of NaCl over the reaction time. When the reaction time was 2 h, Ni<sub>3</sub>S<sub>4</sub>/NiS/NC-2 did not form an obvious sheet-layer structure but the accumulation structure of crystal seeds of Ni<sub>3</sub>S<sub>4</sub> (figure S2(a)). Equations (2) and (4) occur simultaneously in this system under the action of the space-confined effect, which rapidly promoted the emergence of Ni<sub>3</sub>S<sub>4</sub>/NiS heterojunction nanosheets and gradually grew and thickened (figures S2(b) and (c)). The yields of Ni<sub>3</sub>S<sub>4</sub> and NiS increased without transitions to each other for Ni<sub>3</sub>S<sub>4</sub>/NiS/NC-12 to be made of many nanosheets with a smooth surface as the building block (figure S2(d)). When the reaction time was more than 12 h, NiCl<sub>2</sub> near the molten salt interface of recrystallized NaCl was almost completely converted to NiS, and the reaction of excess H<sub>2</sub>S in the closed system and NiS triggered equation (3). However, the ratio of S atoms in Ni<sub>3</sub>S<sub>4</sub> is higher than that in NiS, and the crystal cell parameters of Ni<sub>3</sub>S<sub>4</sub> (cell volume = 0.854 nm<sup>3</sup>,  $a = b = c = 0.9488$  nm,  $\alpha = \beta = \gamma = 90^\circ$ ) are significantly different from those of NiS (cell volume = 0.054 nm<sup>3</sup>,  $a = b = 0.342$  nm and  $c = 0.53$  nm,  $\alpha = \beta = 90^\circ$  and  $\gamma = 120^\circ$ ), leading to the appearance of pulverization on the smooth surface of Ni<sub>3</sub>S<sub>4</sub>/NiS heterojunction nanosheets during the transformation of NiS to Ni<sub>3</sub>S<sub>4</sub> (figures S2(e) and (f)). This phenomenon was improved by increasing the purity of the Ni<sub>3</sub>S<sub>4</sub> in the final material. The thickness of the

building block sheets almost doubled (figure S2(g)), which is the inevitable result of the crystal size of Ni<sub>3</sub>S<sub>4</sub> being larger than that of NiS. In addition, figures 2(b), (c) and S3 display the scanning electron microscopy (SEM) images of Ni<sub>3</sub>S<sub>4</sub>/NiS/NC-12 and Ni<sub>3</sub>S<sub>4</sub>/NC-12. The former presents a relatively uniform micron spherical microstructure with nanosheets as the structural units (figures 2(b), (c) and S3(a)), while the latter shows more than four kinds of microscopic morphologies (figures S3(b)–(f)). The morphological evolution of Ni<sub>3</sub>S<sub>4</sub>/NiS/NC with the reaction time demonstrates that the space-confined effect of recrystallized NaCl is essential for the construction of the Ni<sub>3</sub>S<sub>4</sub>/NiS heterojunction, and the addition of NaCl can contribute to the improvement of the uniformity of the morphology of the final materials.

Transmission electron microscopy (TEM) was performed to investigate the construction interface of the Ni<sub>3</sub>S<sub>4</sub>/NiS/NC heterojunction. Figure 2(d) shows Ni<sub>3</sub>S<sub>4</sub>/NiS/NC-12 with a microspherical structure using nanosheets as the building block, which is consistent with the SEM images. Many nanoparticles with sizes less than 20 nm were riveted on the nanosheets (figure 2(e)), thus exposing a large number of active sites and contributing to the excellent performance of this composite. The high-resolution TEM (HRTEM) image of Ni<sub>3</sub>S<sub>4</sub>/NiS/NC-12 (figure 2(f)) shows clear light-dark lattice fringes in different directions, with a clear lattice distortion interface between them (figure 2(g)). The crystal planes with spacing values of 0.335, 0.237, and 0.296 nm can be assigned to the (2 2 0) and (4 0 0) planes of Ni<sub>3</sub>S<sub>4</sub> and (1 0 0) plane of NiS, which are perpendicular to the plane composed of light

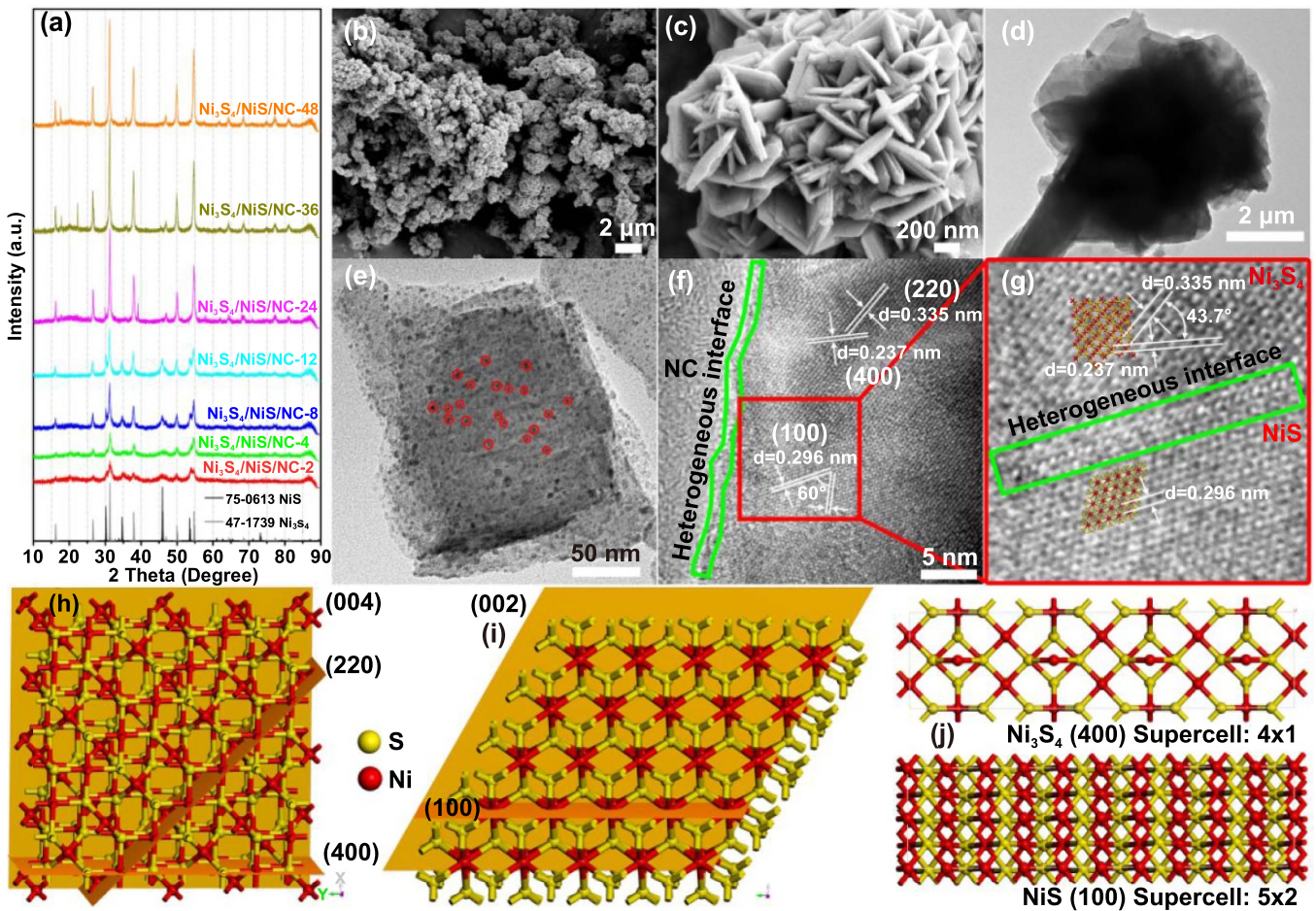


**Figure 2.** (a) XRD patterns of  $\text{Ni}_3\text{S}_4/\text{NiS}/\text{NC}-2$ ,  $\text{Ni}_3\text{S}_4/\text{NiS}/\text{NC}-4$ ,  $\text{Ni}_3\text{S}_4/\text{NiS}/\text{NC}-8$ ,  $\text{Ni}_3\text{S}_4/\text{NiS}/\text{NC}-12$ ,  $\text{Ni}_3\text{S}_4/\text{NiS}/\text{NC}-24$ ,  $\text{Ni}_3\text{S}_4/\text{NiS}/\text{NC}-36$  and  $\text{Ni}_3\text{S}_4/\text{NiS}/\text{NC}-48$ . (b) and (c) SEM images of  $\text{Ni}_3\text{S}_4/\text{NiS}/\text{NC}-12$  with different magnifications. (d) TEM image of the single micro flower of  $\text{Ni}_3\text{S}_4/\text{NiS}/\text{NC}-12$ . (e) TEM image of single nanosheet of  $\text{Ni}_3\text{S}_4/\text{NiS}/\text{NC}-12$ . (f) HRTEM image of  $\text{Ni}_3\text{S}_4/\text{NiS}/\text{NC}-12$ . (g) the larger view of the corresponding red box area in (f). Spatial position simulation of (h) (0 0 4), (2 2 0) and (4 0 0) planes in  $\text{Ni}_3\text{S}_4$ , and (i) (0 0 2) and (1 0 0) planes in NiS. (j) Simulations of supercell crystal face according to the (4 0 0) plane in  $\text{Ni}_3\text{S}_4$  and (1 0 0) plane in NiS.

and dark diffraction spots. The angle between the (4 0 0) and (2 2 0) planes of  $\text{Ni}_3\text{S}_4$  was  $43.7^\circ$ , which was consistent with the angle between the corresponding crystal faces in the simulated crystal structure (figure S4(a)). The planes of the light and dark diffraction spots can be assigned to the (0 0 4) plane of  $\text{Ni}_3\text{S}_4$ , satisfying that it is simultaneously perpendicular to the (4 0 0) and (2 2 0) planes, which is in agreement with the simulation results (figure 2(h)), revealing that the heterogeneous interface of  $\text{Ni}_3\text{S}_4$  is the (4 0 0) plane. Because of the cubic system of  $\text{Ni}_3\text{S}_4$ , the (4 0 0), (0 4 0), and (0 0 4) crystal planes have the same parameters and exhibit a square shape (figures S4(a), (h) and (i)). Similarly, combining the HRTEM image (figure 2(g)) and simulated crystal structure (figure 2(i)) of NiS demonstrates that the plane of the light and dark diffraction spots is the (0 0 2) crystal plane, and the crystal plane perpendicular to the light and dark diffraction spots is the (1 0 0) crystal plane. The heterogeneous interface of NiS is the (1 0 0) plane. Therefore, the heterojunction interface in figure 2(g) was constructed by the (4 0 0) and (1 0 0) planes of  $\text{Ni}_3\text{S}_4$  and NiS, respectively, through the distortion and rearrangement of the corresponding crystal faces.

The hexagonal crystal system of NiS determines the hexagonal crystal plane of (0 0 2) (figure S4(b)) and rectangular plane of (1 0 0) (figure S4(c)). The  $4 \times 1$  supercell of the (4 0 0) square plane of  $\text{Ni}_3\text{S}_4$  and  $5 \times 2$  supercell of the (1 0 0) rectangular plane of NiS exhibit the same rectangular structure with a similar length (approximately 2.67 nm and width of approximately 0.677 nm (figure 2(j)), revealing that the (4 0 0) and (1 0 0) planes of  $\text{Ni}_3\text{S}_4$  and NiS, respectively, have a high matching degree, further proving the feasibility of constructing the  $\text{Ni}_3\text{S}_4/\text{NiS}$  heterojunction. In addition, another heterojunction of the (2 2 0) plane of  $\text{Ni}_3\text{S}_4$  and (1 0 2) plane of NiS can also be observed in figure S4(d), which displays lattice stripes with widths of 0.237 nm and 0.197 nm, corresponding to the (0 4 0) and (1 0 2) planes of  $\text{Ni}_3\text{S}_4$  and NiS, respectively. The angle between the heterogeneous interface and the (0 4 0) plane of  $\text{Ni}_3\text{S}_4$  was approximately  $45^\circ$ , and the heterogeneous interface was parallel to the (1 0 2) plane of NiS. Figure S4(j) exhibits the spatial position simulation of the (0 4 0) and (2 2 0) planes in  $\text{Ni}_3\text{S}_4$ , indicating that the heterogeneous interface of  $\text{Ni}_3\text{S}_4$  is the (2 2 0) plane. This heterojunction was assembled from the (2 2 0) (1 0 2) planes of

$\text{Ni}_3\text{S}_4$  (figure S4(k)) and NiS (figure S4(l)). They were all rectangular crystal faces, showing a high degree of matching for constructing the heterogeneous interface. It can be concluded that  $\text{Ni}_3\text{S}_4/\text{NiS}$  heterojunction materials with different types of heterogeneous interfaces were successfully constructed by the space-confined effect of the recrystallization NaCl melt interface. These different types of heterogeneous interfaces have defects induced by crystal face distortion and lattice dislocation, as well as the rearrangement of electrons at the interface, resulting in the unique electrochemical performance of the heterojunction interfaces [36–38]. The clear boundary verifies the formation of an intimate contact interface (figures 2(f), S4(d) and (f)) between the legible lattice fringe from nickel sulfides and typical amorphous structure of NC. Meanwhile, the discontinued lattice fringe of  $\text{Ni}_3\text{S}_4/\text{NiS}/\text{NC}$ -12 confirmed that there were defects [27]. The corresponding selected area electron diffraction pattern in figure S4(e) shows several diffraction rings composed of diffraction bright spots, matching the (1 0 2) plane of NiS and (0 4 0) and (2 2 0) planes of  $\text{Ni}_3\text{S}_4$ , which further supports the conclusion of the above heterogeneous interface. Figures S4(f) and (g) present a clear lattice spacing of 0.547 nm and distinct diffraction spots, both of which are assigned to the (1 1 1) plane of  $\text{Ni}_3\text{S}_4$  and reveal the excellent crystallinity of  $\text{Ni}_3\text{S}_4$ .

The elemental maps in figures 3(a) and (b) present the distributions of Ni, S, C, and N. To avoid the signal interference of C and N caused by the introduction of a conductive agent during sample preparation,  $\text{Ni}_3\text{S}_4/\text{NiS}/\text{NC}$ -12 was dispersed in an appropriate amount of ethanol by ultrasound and then coated on a glass sheet for energy-dispersive spectroscopy (EDS) testing. The intensity and position of each element distribution shows that this composite mainly contains Ni and S as well as small amounts of C and N, further proving that the as-obtained  $\text{Ni}_3\text{S}_4/\text{NiS}/\text{NC}$ -12 is composed of  $\text{Ni}_3\text{S}_4$ , NiS, and NC. To further determine the form of each element, XPS was employed to investigate the elemental composition and chemical states of the surface of  $\text{Ni}_3\text{S}_4/\text{NiS}/\text{NC}$ -12 (figures S5 and 3(c)–(f)). The survey scan spectrum again indicated the coexistence of Ni, S, C, and N, which was in good agreement with the EDS results. The unexpected O 1s peak may be caused by the partial oxidation of the surface of the sample [39–41]. The Cl 1s and Cl 2s peaks may have been triggered by residual Cl coordination in the sample. High-resolution Ni 2p, S 2p, C 1s, and N 1s curves were obtained through Gaussian fitting. As shown in figure 3(c), the Ni 2p spectrum could be divided into two pairs of shake-up satellites (denoted as ‘Sat.’) (Located at 861.0 and 877.6 eV and 864.7 and 881.8 eV) and two pairs of spin-orbit doublets corresponding to Ni 2p<sub>3/2</sub> and Ni 2p<sub>1/2</sub> of Ni<sup>2+</sup> (853.4 and 871.2 eV) and Ni<sup>3+</sup> (855.6 and 873.3 eV) [16, 42–45]. Ni<sup>2+</sup> is distributed in NiS and  $\text{Ni}_3\text{S}_4$ , whereas Ni<sup>3+</sup> is only distributed in  $\text{Ni}_3\text{S}_4$ . In figure 3(d), the high-resolution S 2p spectrum can be deconvoluted into four peaks, in which the peaks at 161.4 and 162.8 eV correspond to S 2p<sub>3/2</sub> and S 2p<sub>1/2</sub> of S<sup>2-</sup> [43], respectively, and the other two peaks located at 163.9 and 168.8 eV are attributed to the S–C bonds (163.9 eV) [46] and oxidation of NiS and  $\text{Ni}_3\text{S}_4$  (168.8 eV) [43]. As shown in figure 3(e), the C 1s peak is deconvoluted into three peaks at 284.9, 288.1, and 285.9 eV that correspond

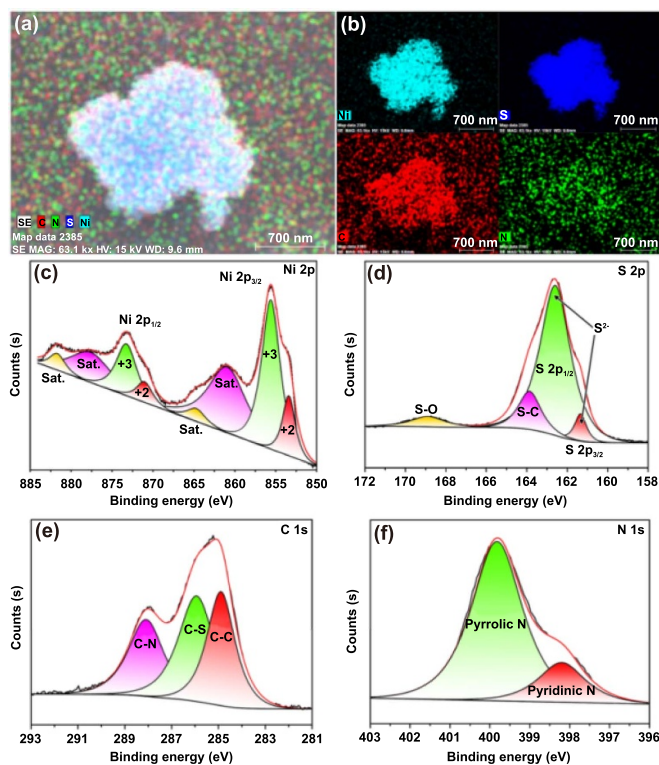


**Figure 3.** (a) and (b) the energy-dispersive spectroscopy (EDS) elemental mapping images of  $\text{Ni}_3\text{S}_4/\text{NiS}/\text{NC}$ -12. High-resolution x-ray photoelectron spectra (XPS) of (c) Ni 2p, (d) S 2p, (e) C 1s and (f) N 1s of  $\text{Ni}_3\text{S}_4/\text{NiS}/\text{NC}$ -12.

to C–C, C–S, and C–N carbons, respectively [39, 41, 46, 47]. The N 1s spectrum (figure 3(f)) is composed of pyridinic N (398.2 eV) and pyrrolic N (399.8 eV) [39, 41, 45], which can create more defects in  $\text{Ni}_3\text{S}_4/\text{NiS}/\text{NC}$ -12 and intensify the kinetics process, providing more reactive active sites for the electrochemical process. The XPS results further confirmed that  $\text{Ni}_3\text{S}_4/\text{NiS}/\text{NC}$ -12 consisted of  $\text{Ni}_3\text{S}_4$ , NiS, and NC.  $\text{Ni}_3\text{S}_4$  and NiS were constructed from rich heterojunctions with different heterogeneous crystal faces. Nickel sulfide is bonded to NC by C–S bonds, which can enhance the heterogeneous interface between nickel sulfide and NC. The local electronic structures of nickel sulfides and NC can be modulated, especially at the interface, which can further accelerate the adsorption and desorption kinetics of electrolyte ions during the electrochemical process [48, 49].

From the above discussion, it can be concluded that the  $\text{Ni}_3\text{S}_4/\text{NiS}/\text{NC}$ -12 composite formed by connecting the  $\text{Ni}_3\text{S}_4/\text{NiS}$  heterojunction and NC through C–S bonds was successfully assembled by the space-confined effect of the molten salt interface of recrystallized NaCl. In view of the multivalent characteristics of nickel ions in nickel sulfides, which have highly reversible redox reactions and are widely applied in the field of supercapacitors,  $\text{Ni}_3\text{S}_4/\text{NiS}/\text{NC}$ -12 and  $\text{Ni}_3\text{S}_4/\text{NC}$ -12 were used as the electrode materials for supercapacitors to investigate the influence of the  $\text{Ni}_3\text{S}_4/\text{NiS}$  heterojunction on electrochemical performance.

The performance of the  $\text{Ni}_3\text{S}_4/\text{NiS}/\text{NC}$ -12 electrode was first examined using a standard three-electrode system in 2M

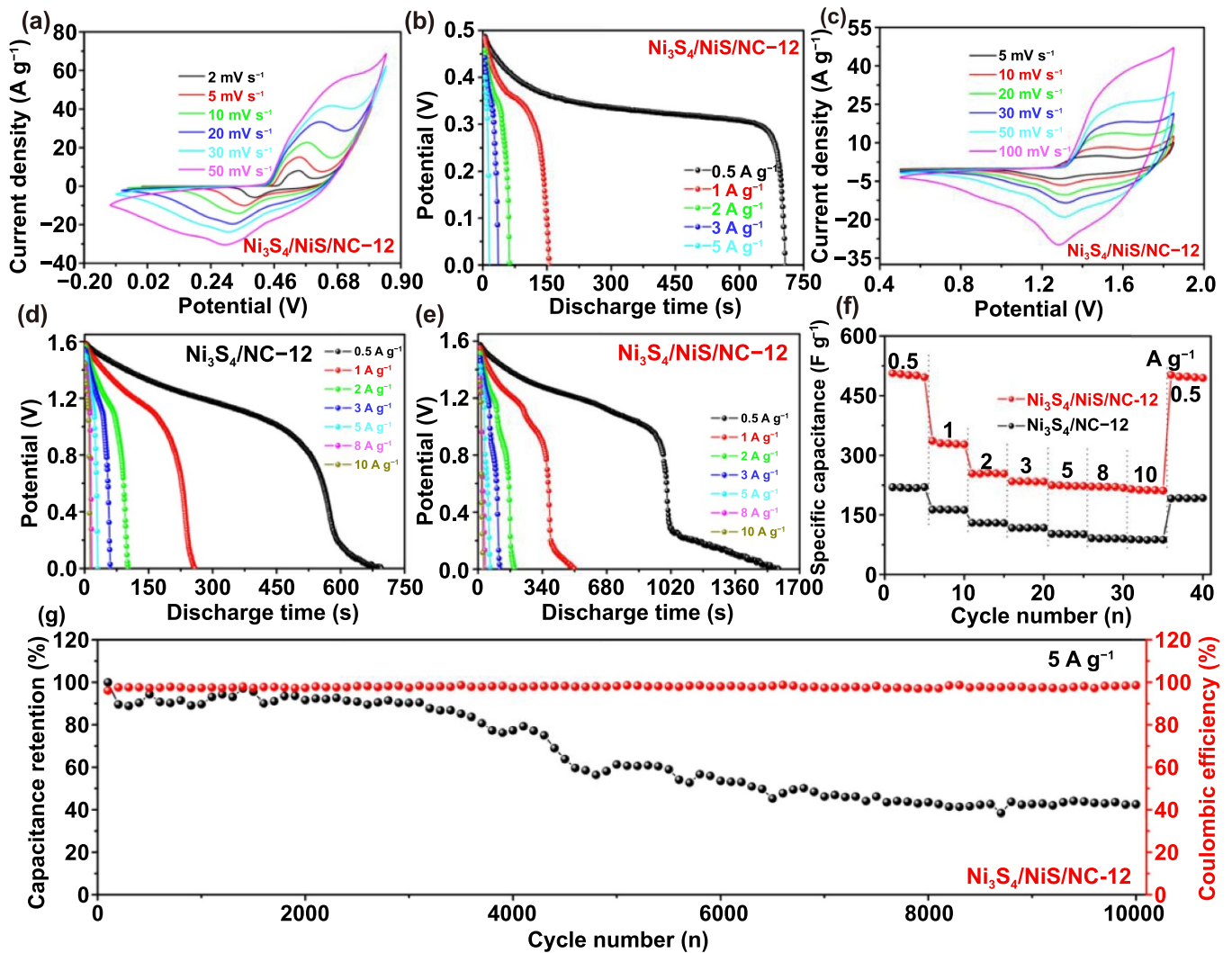


**Figure 4.** Electrochemical performance curves of  $\text{Ni}_3\text{S}_4/\text{NiS}/\text{NC}-12$  in a standard three-electrode system. (a) Cyclic voltammetry (CV) curves at the potential scan rates of 2, 5, 10, 20, 30 and  $50 \text{ mV s}^{-1}$  and (b) galvanostatic discharge curves at  $0.5, 1, 2, 3, 5, 8$  and  $10 \text{ A g}^{-1}$ , respectively. Electrochemical performance curves of the as-assembled devices: (c) CV curves of  $\text{Ni}_3\text{S}_4/\text{NiS}/\text{NC}/\text{AC}$  (AC: active carbon) at 5, 10, 20, 30, 50 and  $100 \text{ mV s}^{-1}$ , galvanostatic discharge curves of (d)  $\text{Ni}_3\text{S}_4/\text{NC}-12//\text{AC}$  and (e)  $\text{Ni}_3\text{S}_4/\text{NiS}/\text{NC}-12//\text{AC}$  at  $0.5, 1, 2, 3, 5, 8$  and  $10 \text{ A g}^{-1}$ , respectively. (f) The corresponding rate performance curves of  $\text{Ni}_3\text{S}_4/\text{NC}-12//\text{AC}$  and  $\text{Ni}_3\text{S}_4/\text{NiS}/\text{NC}-12//\text{AC}$ , and (g) cycle stability curve and coulombic efficiency curve of  $\text{Ni}_3\text{S}_4/\text{NiS}/\text{NC}-12//\text{AC}$  at  $5 \text{ A g}^{-1}$  for 10000 cycles.

KOH. Figure 4(a) presents the typical cyclic voltammetry (CV) curves of  $\text{Ni}_3\text{S}_4/\text{NiS}/\text{NC}-12$  at the potential scan rates of 2, 5, 10, 20, 30, and  $50 \text{ mV s}^{-1}$ . The obvious oxidation and reduction peaks can be mainly ascribed to the reversible redox reaction  $\text{Ni}^{2+} \leftrightarrow \text{Ni}^{3+}$  [13, 15, 16, 50]. The CV curves show no clear shape change with an increasing scan rate, indicating that the heterojunction of  $\text{Ni}_3\text{S}_4/\text{NiS}$  is conducive to high reversibility and fast redox reaction at the interface [51]. The specific capacitances of  $\text{Ni}_3\text{S}_4/\text{NiS}/\text{NC}-12$  (figure S6(a)) at the corresponding scan rate are 635.4, 518.2, 442.5, 377.2, 321.4, and  $263.3 \text{ F g}^{-1}$ , calculated from the CV curves. The distinct discharge platform in the galvanostatic discharge curves (figure 4(b)) and reversible redox peaks in the CV curves prove the outstanding pseudocapacitive properties of  $\text{Ni}_3\text{S}_4/\text{NiS}/\text{NC}-12$ . The specific capacitances of  $\text{Ni}_3\text{S}_4/\text{NiS}/\text{NC}-12$  (figure S6(b)) in figure 4(b) were 644.2,

323.0, 274.3, 232.4, and  $180.5 \text{ F g}^{-1}$  at  $0.5, 1, 2, 3,$  and  $5 \text{ A g}^{-1}$ , respectively. The performance of  $\text{Ni}_3\text{S}_4/\text{NiS}/\text{NC}-12$  with the  $\text{Ni}_3\text{S}_4/\text{NiS}$  heterojunction in a three-electrode system reveals that it has promising applications in the field of supercapacitors.

Asymmetric supercapacitors using  $\text{Ni}_3\text{S}_4/\text{NiS}/\text{NC}-12$  or  $\text{Ni}_3\text{S}_4/\text{NC}-12$  as the working electrodes and activated carbon (AC) as the counter electrode were assembled sequentially to investigate the contribution of the specific capacitance of the  $\text{Ni}_3\text{S}_4/\text{NiS}$  heterojunction. Figure 4(c) shows the CV curves of  $\text{Ni}_3\text{S}_4/\text{NiS}/\text{NC}-12//\text{AC}$  at varying scan rates, which also present obvious redox peaks in good agreement with the CV curves of  $\text{Ni}_3\text{S}_4/\text{NiS}/\text{NC}-12$  in the three-electrode system. In other words, the reversible redox reaction between  $\text{Ni}^{2+}$  and  $\text{Ni}^{3+}$  contributes to the main capacitance. The galvanostatic discharge curves of  $\text{Ni}_3\text{S}_4/\text{NC}-12//\text{AC}$  and

$\text{Ni}_3\text{S}_4/\text{NiS}/\text{NC}-12//\text{AC}$  are presented in figures 4(d) and (e), respectively. The heterojunction of  $\text{Ni}_3\text{S}_4/\text{NiS}$  can optimize the electron configuration in the bulk material and introduce multiple defects owing to crystal face distortion and lattice dislocation, providing more highly active reaction sites for reversible redox reactions and enhancing the kinetic process, which ultimately achieves a longer discharge time of  $\text{Ni}_3\text{S}_4/\text{NiS}/\text{NC}-12//\text{AC}$  than  $\text{Ni}_3\text{S}_4/\text{NC}-12//\text{AC}$  under the same test conditions. The specific capacitances of  $\text{Ni}_3\text{S}_4/\text{NiS}/\text{NC}-12$  in  $\text{Ni}_3\text{S}_4/\text{NiS}/\text{NC}-12//\text{AC}$  are 502.1, 330.3, 254.4, 234.1, 223.5, 220.3, and 213.0  $\text{F g}^{-1}$  at the current densities of 0.5, 1, 2, 3, 5, 8, and 10  $\text{A g}^{-1}$ , respectively, which are more than twice the specific capacitances of  $\text{Ni}_3\text{S}_4/\text{NC}-12$  in  $\text{Ni}_3\text{S}_4/\text{NC}-12//\text{AC}$  at same current densities (figure 4(f)). The capacitance retention ratios of  $\text{Ni}_3\text{S}_4/\text{NiS}/\text{NC}-12$  and  $\text{Ni}_3\text{S}_4/\text{NC}-12$  in the corresponding devices at 0.5  $\text{A g}^{-1}$  before and after the large current cycle are 99.1% and 87.8% (figure 4(f)), respectively, which reveals that the construction of the  $\text{Ni}_3\text{S}_4/\text{NiS}$  heterojunction can also improve the ability to withstand large current charge and discharge. The optimization of the reaction active sites and kinetic process by the  $\text{Ni}_3\text{S}_4/\text{NiS}$  heterojunction can further reduce the uneven deformation of the active material caused by electrochemical polarization during the charge and discharge processes. In addition, the stable composite mode formed by C–S bonds between NC and nickel sulfide can reinforce the mechanical strength of the active materials and inhibit their deformation. Thus, the heterojunctions and C–S bonds can ensure that  $\text{Ni}_3\text{S}_4/\text{NiS}/\text{NC}-12//\text{AC}$  can be tested for 10 000 cycles at 5  $\text{A g}^{-1}$  and maintain 42.6% of the initial capacitance (figure 4(g)). Meanwhile, the coulombic efficiency of  $\text{Ni}_3\text{S}_4/\text{NiS}/\text{NC}-12//\text{AC}$  was always close to 100% over 10 000 cycles, indicating that  $\text{Ni}_3\text{S}_4/\text{NiS}/\text{NC}-12$  exhibits high reversible redox activity.

The energy and power densities calculated from the galvanostatic charge–discharge data of  $\text{Ni}_3\text{S}_4/\text{NiS}/\text{NC}-12//\text{AC}$  are shown in the Ragone plot (figure 5). The  $\text{Ni}_3\text{S}_4/\text{NiS}/\text{NC}-12//\text{AC}$  achieves a high energy density of 60.1  $\text{Wh kg}^{-1}$  at a power density of 142.0  $\text{W kg}^{-1}$  and 16.6  $\text{Wh kg}^{-1}$  at a high power density of 3338.3  $\text{W kg}^{-1}$ . These values are also competitive to other transition-metal-based supercapacitor devices, such as  $\text{NiCo}_2\text{O}_4@\text{NiO}/\text{AC}$  (31.5  $\text{Wh kg}^{-1}$  at 215.2  $\text{W kg}^{-1}$ ) [52],  $(\text{Ni}_{0.1}\text{Co}_{0.9})_9\text{Se}_8@\text{carbon fiber cloth (CFC)}/\text{polyvinyl alcohol}/\text{KOH}/\text{reduced graphene oxide (rGO)}/\text{CFC}$  (17.0  $\text{Wh kg}^{-1}$  at 3100  $\text{W kg}^{-1}$ ) [53],  $\text{Ni}_3\text{S}_4//\text{AC}$  (18.6  $\text{Wh kg}^{-1}$  at 150  $\text{W kg}^{-1}$  and 11.7  $\text{Wh kg}^{-1}$  at 1500.2  $\text{W kg}^{-1}$ ) [54],  $\text{Ni-CoP}@C@\text{carbon nanotube}/\text{graphene (GO)}$  (17.4  $\text{Wh kg}^{-1}$  at 699.1  $\text{W kg}^{-1}$ ) [55],  $\text{O-NiCoP}@r\text{GO}/\text{AC}$  (21  $\text{Wh kg}^{-1}$  at 775  $\text{W kg}^{-1}$ ) [56],  $\text{CoSe}_2//\text{AC}$  (18.9  $\text{Wh kg}^{-1}$  at 387  $\text{W kg}^{-1}$ ) [57],  $\text{CoSe}_2/\text{C}/\text{AC}$  (20.6  $\text{Wh kg}^{-1}$  at 698.8  $\text{W kg}^{-1}$ ) [58], and  $\text{CuCo}_2\text{O}_4/\text{CuO}-400//\text{AC}$  (19.2  $\text{Wh kg}^{-1}$  at 770.4  $\text{W kg}^{-1}$ ) [59]. These combined results demonstrate the outstanding performance of  $\text{Ni}_3\text{S}_4/\text{NiS}/\text{NC}-12//\text{AC}$  in practical applications.

To further elucidate the origin of the enhanced electrochemical performance of  $\text{Ni}_3\text{S}_4/\text{NiS}/\text{NC}-12$ , DFT calculations were performed to investigate its conductivity. The optimized model of the  $\text{Ni}_3\text{S}_4/\text{NiS}$  heterojunction is shown in figure S7,

which clearly reveals the formation of stable Ni–S bonds between  $\text{Ni}_3\text{S}_4$  and NiS. The DOS profiles based on the optimized  $\text{Ni}_3\text{S}_4/\text{NiS}$  heterojunction are shown in figures 5(b) and (c). The partial density of state (PDOS) profile of the *d*-state of Ni and *p*-state of S presented a larger DOS area (figure 5(b)) at the Fermi level, confirming that new chemical bonds were formed between Ni and S. Because the Fermi–Dirac difference has a high value as it approaches the Fermi level, a high DOS near the Fermi level can result in excellent electronic properties [51]. The DOS analysis of the  $\text{Ni}_3\text{S}_4/\text{NiS}$  heterojunction (figure 5(c)) demonstrates that the heterogeneous interface of  $\text{Ni}_3\text{S}_4/\text{NiS}$  can exhibit a metallic character, induce active electron-transfer dynamics, and produce outstanding electronic properties; thus, the  $\text{Ni}_3\text{S}_4/\text{NiS}$  heterojunction has a relatively high conductivity for facilitating electron transfer [51, 60]. The electron density difference of the  $\text{Ni}_3\text{S}_4/\text{NiS}$  heterojunction model was also determined to characterize the nature of the interactions (figure 5(d)). The blue and purple regions refer to electron accumulation and depletion, respectively. The electrons were redistributed at the heterogeneous interface between  $\text{Ni}_3\text{S}_4$  and NiS. The electrons can be transferred from  $\text{Ni}_3\text{S}_4$  to NiS at the heterogeneous interface according to the Bader charge analysis results, which strengthens the electronic interaction between  $\text{Ni}_3\text{S}_4$  and NiS and the stability of the interfacial connection [27, 61]. The electrical interaction at the heterogeneous interface can contribute to high electronic conductivity, which can become a good electroactive area for outstanding electrochemical performance.

The above analysis clearly indicates that the enhancement in supercapacitor performance is closely related to the construction of heterojunctions by the space-confined effect of the molten salt interface of recrystallized NaCl. An underlying mechanism is proposed, as illustrated in figure 5(e). It is well known that the ionic and electronic transport efficiencies during the charging and discharging processes are key factors in determining the utilization and electrochemical performance of active materials. In electrochemical energy storage devices, the fluid electrolyte can fully contact the surface of the active electrode materials to improve the contact area between the active material and electrolyte through micro–nano construction technology.  $\text{Ni}_3\text{S}_4/\text{NiS}/\text{NC}-12$  material using nanosheets as the building block can provide a rich electrode–electrolyte interface supplying sufficient channels for ion transfer between  $\text{Ni}_3\text{S}_4/\text{NiS}/\text{NC}-12$  and the electrolyte. However, the surface of a solid-state active material with a micro–nano structure is difficult to completely cover using a solid-state current collector or a material with high electronic conductivity. When the surface area of the active material is constant, increasing the solid–solid interface can reduce the electrode–electrolyte interface area. Therefore, the electronic transmission efficiency can be effectively improved by improving the electronic conductivity of the active materials. To this end,  $\text{Ni}_3\text{S}_4/\text{NiS}/\text{NC}-12$  constructed with multiple heterojunctions can provide a 3D conductive network by the chelation of highly conductive NC with nickel sulfide and the unique electrical interaction at the  $\text{Ni}_3\text{S}_4/\text{NiS}$

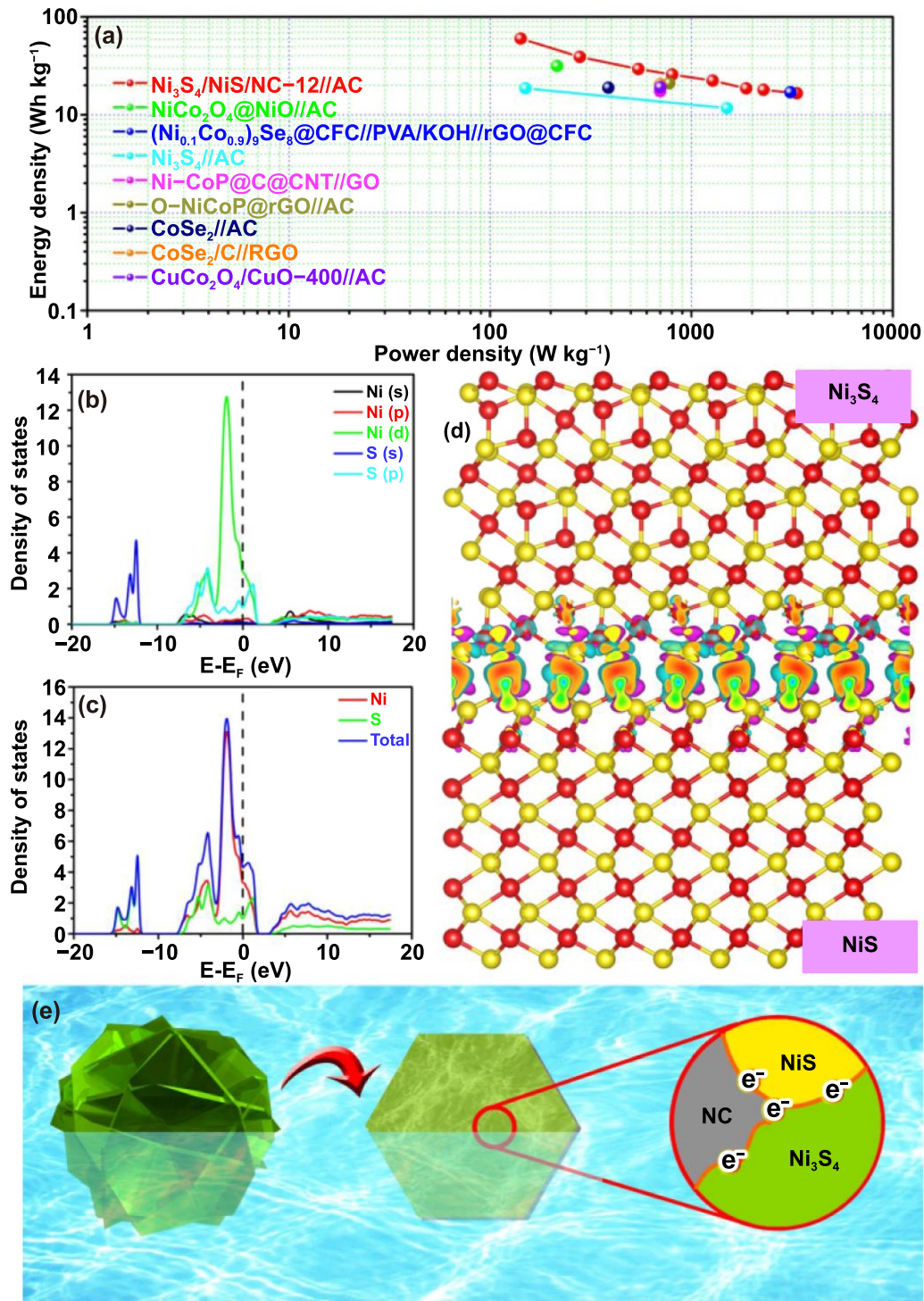


**Figure 5.** (a) Ragone plot correlating the energy densities and power densities of Ni<sub>3</sub>S<sub>4</sub>/NiS/NC-12//AC (b) partial density of states (PDOSs) and (c) local density of states (LDOSs) and total density of states (TDOS) of Ni<sub>3</sub>S<sub>4</sub>/NiS heterojunction. (d) Electron density difference plots at the interface of Ni<sub>3</sub>S<sub>4</sub>/NiS heterojunction. (e) Structure-activity relationship schematic of the contribution of microstructure and multiple heterojunctions of Ni<sub>3</sub>S<sub>4</sub>/NiS/NC-12 to electrochemical performance.

heterogeneous interface. NC can limit the structural deformation of nickel sulfides caused by reversible redox reactions, and the construction of multiple heterogeneous interfaces and N-doping introduces many defects and highly active sites in Ni<sub>3</sub>S<sub>4</sub>/NiS/NC-12, which contribute to the improvement of the structural stability and electrochemical performance.

### 3. Conclusions

In conclusion, the one-step preparation technique of Ni<sub>3</sub>S<sub>4</sub>/NiS/NC multiple heterojunction nanosheets is innovatively designed using the space-confined effect of the molten salt interface of recrystallized NaCl. The C-S bonds between

NC and nickel sulfides and the Ni–S bonds between Ni<sub>3</sub>S<sub>4</sub> and NiS can strengthen the stability of multiple heterojunctions with many defects and highly active sites for enhancing electron and ion transport kinetics. The synergy between the high electronic conductivity of NC and electron interaction of the Ni<sub>3</sub>S<sub>4</sub>/NiS heterogeneous interface work together to weave rich heterogeneous interfaces into the 3D conductive network as interconnected electronic transport channels inside the Ni<sub>3</sub>S<sub>4</sub>/NiS/NC-12 electrode material, which enhances electronic transmission within the material. The resulting Ni<sub>3</sub>S<sub>4</sub>/NiS/NC-12 exhibited more than twice the specific capacitance of Ni<sub>3</sub>S<sub>4</sub>/NC-12 prepared without NaCl. The as-assembled Ni<sub>3</sub>S<sub>4</sub>/NiS/NC-12//AC asymmetric supercapacitor exhibits a high energy density of 60.1 Wh kg<sup>-1</sup> at a power density of 142.0 W kg<sup>-1</sup> and 16.6 Wh kg<sup>-1</sup> at a high power density of 3338.3 W kg<sup>-1</sup>. The Ni<sub>3</sub>S<sub>4</sub>/NiS/NC multiple heterojunction nanosheets were demonstrated to have considerable potential for use in advanced electrochemical energy storage devices; the synthetic method based on the NaCl-based space-confined effect can be extended to the preparation of other heterogeneous materials.

## Acknowledgments

This work was supported by the National Natural Science Foundation of China (Grant Nos. U1804126, U21A2077 and U1804129), the Support Program of Science and Technology Innovation Leading Talent of Zhongyuan (Grant 204200510014), PhD program of Shanghai University and Program for Interdisciplinary Direction Team in Zhongyuan University of Technology.

## ORCID iD

Jiujun Zhang  <https://orcid.org/0000-0002-6858-4060>

## References

- [1] Simon P and Gogotsi Y 2008 Materials for electrochemical capacitors *Nat. Mater.* **7** 845–54
- [2] Wu F, Liu M Q, Li Y, Feng X, Zhang K, Bai Y, Wang X R and Wu C 2021 High-mass-loading electrodes for advanced secondary batteries and supercapacitors *Electrochem. Energy Rev.* **4** 382–446
- [3] Duan J, Tang X, Dai H F, Yang Y, Wu W Y, Wei X Z and Huang Y H 2020 Building safe lithium-ion batteries for electric vehicles: a review *Electrochem. Energy Rev.* **3** 1–42
- [4] Wu D, Peng C, Yin C and Tang H 2020 Review of system integration and control of proton exchange membrane fuel cells *Electrochem. Energy Rev.* **3** 466–505
- [5] Seh Z W, Kibsgaard J, Dickens C F, Chorkendorff I, Nørskov J K and Jaramillo T F 2017 Combining theory and experiment in electrocatalysis: insights into materials design *Science* **355** eaad4998
- [6] Wei W T, Xu J Q, Chen W H, Mi L W and Zhang J J 2022 A review of sodium chloride-based electrolytes and materials for electrochemical energy technology *J. Mater. Chem. A* **10** 2637–71
- [7] Wu H M, Feng C Q, Zhang L, Zhang J J and Wilkinson D P 2021 Non-noble metal electrocatalysts for the hydrogen evolution reaction in water electrolysis *Electrochem. Energy Rev.* **4** 473–507
- [8] Zheng Y, Chen Z W and Zhang J J 2021 Solid oxide electrolysis of H<sub>2</sub>O and CO<sub>2</sub> to produce hydrogen and low-carbon fuels *Electrochem. Energy Rev.* **4** 508–17
- [9] Pan J Q, Wang P H, Wang P P, Yu Q, Wang J J, Song C S, Zheng Y Y and Li C R 2021 The photocatalytic overall water splitting hydrogen production of g-C<sub>3</sub>N<sub>4</sub>/CdS hollow core-shell heterojunction via the HER/OER matching of Pt/MnO<sub>x</sub> *Chem. Eng. J.* **405** 126622
- [10] Madhusudan P, Shi R, Xiang S L, Jin M T, Chandrashekar B N, Wang J W, Wang W J, Peng O W, Amini A and Cheng C 2021 Construction of highly efficient Z-scheme Zn<sub>x</sub>Cd<sub>1-x</sub>S/Au@g-C<sub>3</sub>N<sub>4</sub> ternary heterojunction composite for visible-light-driven photocatalytic reduction of CO<sub>2</sub> to solar fuel *Appl. Catal. B* **282** 119600
- [11] Ye J et al 2021 Novel N-Black In<sub>2</sub>O<sub>3-x</sub>/InVO<sub>4</sub> heterojunction for efficient photocatalytic fixation: synergistic effect of exposed (321) facet and oxygen vacancy *J. Mater. Chem. A* **9** 24600–12
- [12] Song X et al 2021 Synergistic interplay between asymmetric backbone conformation, molecular aggregation, and charge-carrier dynamics in fused-ring electron acceptor-based bulk heterojunction solar cells *ACS Appl. Mater. Interfaces* **13** 2961–70
- [13] Wei W T, Wu J R, Cui S Z, Zhao Y M, Chen W H and Mi L W 2019  $\alpha$ -Ni(OH)<sub>2</sub>/NiS<sub>1.97</sub> heterojunction composites with excellent ion and electron transport properties for advanced supercapacitors *Nanoscale* **11** 6243–53
- [14] Yang H F, Guo H R, Li X P, Ren W L and Song R 2021 Regulation effects of Co<sup>2+</sup> on the construction of a Cu-Ni(OH)<sub>2</sub>@CoO nanoflower cluster heterojunction: a critical factor in obtaining a high-performance battery-type hybrid supercapacitor *Nanoscale* **13** 18182–91
- [15] Yu S, Xiong X B, Ma J and Qian H X 2021 One-step preparation of cobalt nickel oxide hydroxide@cobalt sulfide heterostructure film on Ni foam through hydrothermal electrodeposition for supercapacitors *Surf. Coat. Technol.* **426** 127791
- [16] Song K, Li W T, Yang R, Zheng Y J, Chen X S, Wang X, Chen G L and Lv W C 2021 Controlled preparation of Ni(OH)<sub>2</sub>/NiS nanosheet heterostructure as hybrid supercapacitor electrodes for high electrochemical performance *Electrochim. Acta* **388** 138663
- [17] Zhang Y F, Zhu Y K, Lv C X, Lai S J, Xu W J, Sun J, Sun Y Y and Yang D J 2020 Enhanced visible-light photoelectrochemical performance via chemical vapor deposition of Fe<sub>2</sub>O<sub>3</sub> on a WO<sub>3</sub> film to form a heterojunction *Rare Met.* **39** 841–9
- [18] Kim Y, Kwon S, Seo E J, Nam J H, Jang H Y, Kwon S H, Kwon J D, Kim D W and Cho B 2018 Facile fabrication of a two-dimensional TMD/Si heterojunction photodiode by atmospheric-pressure plasma-enhanced chemical vapor deposition *ACS Appl. Mater. Interfaces* **10** 36136–43
- [19] Jiamprasertboon A, Kafizas A, Sachs M, Ling M, Alotaibi A M, Lu Y, Siritanon T, Parkin I P and Carmalt C J 2019 Heterojunction  $\alpha$ -Fe<sub>2</sub>O<sub>3</sub>/ZnO films with enhanced photocatalytic properties grown by aerosol-assisted chemical vapour deposition *Chem. Eur. J.* **25** 11337–45
- [20] Patil R P, Mahadik M A, Bae H S, Chae W S, Choi S H and Jang J S 2020 Porous Zn<sub>1-x</sub>Cd<sub>x</sub>S nanosheets/ZnO nanorod heterojunction photoanode via self-templated and cadmium ions exchanged conversion of ZnS(HDA)<sub>0.5</sub> nanosheets/ZnO nanorod *Chem. Eng. J.* **402** 126153
- [21] Qin Y et al 2021 Single-atom-based heterojunction coupling with ion-exchange reaction for sensitive photoelectrochemical immunoassay *Nano Lett.* **21** 1879–87
- [22] Li Y T, Liu Z F, Li J W, Ruan M N and Guo Z G 2020 An effective strategy of constructing a multi-junction structure

- by integrating a heterojunction and a homojunction to promote the charge separation and transfer efficiency of  $\text{WO}_3$ . *J. Mater. Chem. A* **8** 6256–67
- [23] Lu M F, Li Q Q, Zhang C L, Fan X X, Li L, Dong Y M, Chen G Q and Shi H F 2020 Remarkable photocatalytic activity enhancement of  $\text{CO}_2$  conversion over 2D/2D g- $\text{C}_3\text{N}_4/\text{BiVO}_4$  Z-scheme heterojunction promoted by efficient interfacial charge transfer *Carbon* **160** 342–52
- [24] Qiu B C, Zhu Q H, Du M M, Fan L G, Xing M Y and Zhang J L 2017 Efficient solar light harvesting  $\text{CdS}/\text{Co}_9\text{S}_8$  hollow cubes for Z-scheme photocatalytic water splitting *Angew. Chem., Int. Ed.* **56** 2684–8
- [25] Wang M, Tan G Q, Dang M Y, Wang Y, Zhang B X, Ren H J, Lv L and Xia A 2021 Dual defects and build-in electric field mediated direct Z-scheme  $\text{W}_{18}\text{O}_{49}/\text{g-C}_3\text{N}_{4-x}$  heterojunction for photocatalytic NO removal and organic pollutant degradation *J. Colloid Interface Sci.* **582** 212–26
- [26] Li X B et al 2021 Enhanced photocatalytic degradation and  $\text{H}_2/\text{H}_2\text{O}_2$  production performance of S-pCN/ $\text{WO}_{2.72}$  S-scheme heterojunction with appropriate surface oxygen vacancies *Nano Energy* **81** 105671
- [27] Tan M X et al 2022 Boosting photocatalytic hydrogen production via interfacial engineering on 2D ultrathin Z-scheme  $\text{ZnIn}_2\text{S}_4/\text{g-C}_3\text{N}_4$  heterojunction *Adv. Funct. Mater.* **32** 2111740
- [28] Midya A, Ghorai A, Mukherjee S, Maiti R and Ray S K 2016 Hydrothermal growth of few layer 2H- $\text{MoS}_2$  for heterojunction photodetector and visible light induced photocatalytic applications *J. Mater. Chem. A* **4** 4534–43
- [29] Lu X Y, Che W J, Hu X F, Wang Y, Zhang A T, Deng F, Luo S L and Dionysiou D D 2019 The facile fabrication of novel visible-light-driven Z-scheme  $\text{CuInS}_2/\text{Bi}_2\text{WO}_6$  heterojunction with intimate interface contact by *in situ* hydrothermal growth strategy for extraordinary photocatalytic performance *Chem. Eng. J.* **356** 819–29
- [30] Fei F C et al 2015 Solvothermal synthesis of lateral heterojunction  $\text{Sb}_2\text{Te}_3/\text{Bi}_2\text{Te}_3$  nanoplates *Nano Lett.* **15** 5905–11
- [31] Pang H, Li X R, Zhao Q X, Xue H G, Lai W Y, Hu Z and Huang W 2017 One-pot synthesis of heterogeneous  $\text{Co}_3\text{O}_4$ -nanocube/ $\text{Co}(\text{OH})_2$ -nanosheet hybrids for high-performance flexible asymmetric all-solid-state supercapacitors *Nano Energy* **35** 138–45
- [32] Lin Y et al 2019 Construction of CoP/NiCoP nanotadpoles heterojunction interface for wide pH hydrogen evolution electrocatalysis and supercapacitor *Adv. Energy Mater.* **9** 1901213
- [33] Li L, Zhou Y M, Zhou H, Qu H N, Zhang C L, Guo M X, Liu X Q, Zhang Q Y and Gao B 2019 N/P codoped porous carbon/one-dimensional hollow tubular carbon heterojunction from biomass inherent structure for supercapacitors *ACS Sustain. Chem. Eng.* **7** 1337–46
- [34] Luo W H, Zhang G F, Cui Y X, Sun Y, Qin Q, Zhang J and Zheng W J 2017 One-step extended strategy for the ionic liquid-assisted synthesis of  $\text{Ni}_3\text{S}_4$ - $\text{MoS}_2$  heterojunction electrodes for supercapacitors *J. Mater. Chem. A* **5** 11278–85
- [35] Chen P, Cao C B, Ding C S, Yin Z Z, Qi S H, Guo J, Zhang M and Sun Z Q 2022 One-body style photo-supercapacitors based on  $\text{Ni}(\text{OH})_2/\text{TiO}_2$  heterojunction array: high specific capacitance and ultra-fast charge/discharge response *J. Power Sources* **521** 230920
- [36] Zhang T D, Li W L, Zhao Y, Yu Y and Fei W D 2018 High energy storage performance of opposite double-heterojunction ferroelectricity-insulators *Adv. Funct. Mater.* **28** 1706211
- [37] Ou X, Xiao Z M, Zhang J F, Wang C H, Wang D, Zhang B and Wu Y P 2020 Enhancing the rapid  $\text{Na}^+$ -storage performance via electron/ion bridges through  $\text{GeS}_2/\text{graphene}$  heterojunction *ACS Nano* **14** 13952–63
- [38] Zhu S et al 2022 In situ architecting endogenous heterojunction of  $\text{MoS}_2$  coupling with  $\text{Mo}_2\text{CT}_x$  MXenes for optimized  $\text{Li}^+$  storage *Adv. Mater.* **34** 2270036
- [39] Yang J, Xing S Q, Zhou J B, Cheng Y, Shi L and Yang Q 2019 The controlled construction of a ternary hybrid of monodisperse  $\text{Ni}_3\text{S}_4$  nanorods/graphitic  $\text{C}_3\text{N}_4$  nanosheets/nitrogen-doped graphene in van der Waals heterojunctions as a highly efficient electrocatalyst for overall water splitting and a promising anode material for sodium-ion batteries *J. Mater. Chem. A* **7** 3714–28
- [40] Wan K, Luo J S, Zhou C, Zhang T, Arbiol J, Lu X H, Mao B W, Zhang X and Fransaer J 2019 Hierarchical porous  $\text{Ni}_3\text{S}_4$  with enriched high-valence Ni sites as a robust electrocatalyst for efficient oxygen evolution reaction *Adv. Funct. Mater.* **29** 1900315
- [41] Li T F, Lu T Y, Li Y, Yin J W, Tang Y W, Zhang M Y, Pang H, Xu L, Yang J and Zhang Y W 2022 Interfacial engineering-induced electronic regulation drastically enhances the electrocatalytic oxygen evolution: immobilization of Janus-structured NiS/NiO nanoparticles onto carbon nanotubes/nanofiber-integrated superstructures *Chem. Eng. J.* **428** 131094
- [42] Jiang D G, Liang H, Yang W R, Liu Y, Cao X Y, Zhang J M, Li C W, Liu J Q and Gooding J J 2019 Screen-printable films of graphene/ $\text{CoS}_2/\text{Ni}_3\text{S}_4$  composites for the fabrication of flexible and arbitrary-shaped all-solid-state hybrid supercapacitors *Carbon* **146** 557–67
- [43] Wei W T, Ye W Y, Wang J, Huang C, Xiong J B, Qiao H J, Cui S Z, Chen W H, Mi L W and Yan P F 2019 Hydrangea-like  $\alpha\text{-Ni}_{1/3}\text{Co}_{2/3}(\text{OH})_2$  reinforced by ethyl carbamate “Rivet” for all-solid-state supercapacitors with outstanding comprehensive performance *ACS Appl. Mater. Interfaces* **11** 32269–81
- [44] Zhang J X, Deng Y, Wu Y Q, Xiao Z Y, Liu X B, Li Z J, Bu R R, Zhang Q, Sun W and Wang L 2022 Chemically coupled 0D-3D hetero-structure of  $\text{Co}_9\text{S}_8$ - $\text{Ni}_3\text{S}_4$  hollow spheres for Zn-based supercapacitors *Chem. Eng. J.* **430** 132836
- [45] Yang F, Wang S G, Guan J D, Shao L Y, Shi X Y, Cai J J and Sun Z P 2021 Hierarchical  $\text{MoS}_2$ -NiS nanosheet-based nanotubes@N-doped carbon coupled with ether-based electrolytes towards high-performance Na-ion batteries *J. Mater. Chem. A* **9** 27072–83
- [46] Huang C, Gao A M, Yi F Y, Wang Y C, Shu D, Liang Y S, Zhu Z H, Ling J Z and Hao J N 2021 Metal organic framework derived hollow NiS@C with S-vacancies to boost high-performance supercapacitors *Chem. Eng. J.* **419** 129643
- [47] Hegazy M B Z, Berber M R, Yamauchi Y, Pakdel A, Cao R and Apfel U P 2021 Synergistic electrocatalytic hydrogen evolution in Ni/NiS nanoparticles wrapped in multi-heteroatom-doped reduced graphene oxide nanosheets *ACS Appl. Mater. Interfaces* **13** 34043–52
- [48] Tong H G, Wang C L, Lu J, Chen S, Yang K, Huang M X, Yuan Q and Chen Q W 2020 Energetic metal-organic frameworks derived highly nitrogen-doped porous carbon for superior potassium storage *Small* **16** 2002771
- [49] Lu Q, Wu H, Zheng X R, Chen Y N, Rogach A L, Han X P, Deng Y D and Hu W B 2021 Encapsulating cobalt nanoparticles in interconnected N-doped hollow carbon nanofibers with enriched Co-N-C moiety for enhanced oxygen electrocatalysis in Zn-air batteries *Adv. Sci.* **8** 2101438
- [50] Wei W T, Chen W H, Mi L W, Xu J Q and Zhang J J 2021 High-rate performance aqueous-based supercapacitors at  $-30^\circ\text{C}$  driven by novel 1D  $\text{Ni}(\text{OH})_2$  nanorods and a two-solute electrolyte *J. Mater. Chem. A* **9** 23860–72

- [51] Kavinkumar T, Seenivasan S, Lee H H, Jung H, Han J W and Kim D H 2021 Interface-modulated uniform outer nanolayer: a category of electrodes of nanolayer-encapsulated core-shell configuration for supercapacitors *Nano Energy* **81** 105667
- [52] Liu X J, Liu J F and Sun X M 2015 NiCo<sub>2</sub>O<sub>4</sub>@NiO hybrid arrays with improved electrochemical performance for pseudocapacitors *J. Mater. Chem. A* **3** 13900–5
- [53] Yang P Y, Wu Z Y, Jiang Y C, Pan Z C, Tian W C, Jiang L and Hu L F 2018 Fractal (Ni<sub>x</sub>Co<sub>1-x</sub>)<sub>9</sub>Se<sub>8</sub> nanodendrite arrays with highly exposed (01̄) surface for wearable, all-solid-state supercapacitor *Adv. Energy Mater.* **8** 1801392
- [54] Wang H Y, Liang M M, Duan D, Shi W Y, Song Y Y and Sun Z B 2018 Rose-like Ni<sub>3</sub>S<sub>4</sub> as battery-type electrode for hybrid supercapacitor with excellent charge storage performance *Chem. Eng. J.* **350** 523–33
- [55] Gu J L, Sun L, Zhang Y X, Zhang Q Y, Li X W, Si H C, Shi Y, Sun C, Gong Y and Zhang Y H 2020 MOF-derived Ni-doped CoP@C grown on CNTs for high-performance supercapacitors *Chem. Eng. J.* **385** 123454
- [56] Zhang Y X, Sun L, Zhang L K, Li X W, Gu J L, Si H C, Wu L, Shi Y, Sun C and Zhang Y H 2020 Highly porous oxygen-doped NiCoP immobilized in reduced graphene oxide for supercapacitive energy storage *Composites B* **182** 107611
- [57] Liu S X, Sarwar S, Wang J Y, Zhang H P, Li T B, Luo J J and Zhang X Y 2021 The microwave synthesis of porous CoSe<sub>2</sub> nanosheets for super cycling performance supercapacitors *J. Mater. Chem. C* **9** 228–37
- [58] Wang H, Shu T, Yuan J Z, Li Y X, Lin B, Wei F X, Qi J Q and Sui Y 2022 Highly stable lamellar array composed of CoSe<sub>2</sub> nanoparticles for supercapacitors *Colloids Surf. A* **633** 127789
- [59] Liu X H, Sun J L, Liu Y F, Liu D S, Xu C J and Chen H Y 2022 The CuCo<sub>2</sub>O<sub>4</sub>/CuO composite-based microspheres serve as a battery-type cathode material for highly capable hybrid supercapacitors *J. Alloys Compd.* **894** 162566
- [60] Liu S D, Kang L, Hu J S, Jung E, Zhang J, Jun S C and Yamauchi Y 2021 Unlocking the potential of oxygen-deficient copper-doped Co<sub>3</sub>O<sub>4</sub> nanocrystals confined in carbon as an advanced electrode for flexible solid-state supercapacitors *ACS Energy Lett.* **6** 3011–9
- [61] Wang H Q, Zhang W J, Zhang X W, Hu S X, Zhang Z C, Zhou W J and Liu H 2021 Multi-interface collaboration of graphene cross-linked NiS-NiS<sub>2</sub>-Ni<sub>3</sub>S<sub>4</sub> polymorph foam towards robust hydrogen evolution in alkaline electrolyte *Nano Res.* **14** 4857–64